Two-phase flow modeling for the cathode side of a polymer electrolyte fuel cell

Chaozhong Qin [a,b], Dirk Rensink [a,*], Stephan Fell [a], S. Majid Hassanizadeh [b]

[a] *Adam Opel AG, GME Engineering, GM Alternative Propulsion Europe, IPC MK-01, D-65423 Rüsselsheim, Germany*
[b] *Department of Earth Sciences, Utrecht University, P.O. Box 80021, 3508 Utrecht, The Netherlands*

ARTICLE INFO

ABSTRACT

Liquid water flooding in micro gas channels is an important issue in the water management of polymer electrolyte fuel cells (PEFCs). However, in most previous numerical studies liquid water transport in the gas channels (GC) has been simplified by the mist flow assumption. In this work, we present a two-phase flow model for the cathode side of a PEFC. The GC is assumed to be a structured porous medium with the porosity of 1.0. The two-phase Darcy's law is applied to both diffusion layers and GC. Based on the developed model, the liquid water flooding in the GC and its impact on the liquid water distribution in the diffusion layers are explored in detail. Furthermore, we study the effect of the immobile saturation on the predicted liquid water distribution in the diffusion layers. The results show that neglecting the GC flooding leads to an incorrect prediction of liquid water distribution in the diffusion layers and an overestimation of the cell performance. The gas flow rate in the GC can be optimized to achieve the best cell performance. Finally, when considering the immobile saturation in the model, more liquid water is predicted in the diffusion layers.

© 2011 Elsevier B.V. All rights reserved.

1. Introduction

In the pursuit of reduced dependence on fossil fuels, less pollution, as well as high efficiency, the polymer electrolyte fuel cell (PEFC) is regarded as one of the most promising alternative power sources in the future. It is expected to be widely employed in stationary, automotive and portable sections. However, before this can occur, several technical challenges of PEFCs must be solved, such as cell durability, system power density, fuel storage, generation and delivery, as well as system cost to ensure a proper market penetration [1–3].

In a single PEFC unit, various transport processes are intricately coupled, along with electrochemical reactions in the catalyst layers. As a consequence, water and heat issues are always ineluctable. A typical PEFC consists of four distinct constituents, namely, bipolar plate (gas channels are grooved on both sides of bipolar plate), gas diffusion layer (including the micro porous layer), catalyst layer, and polymer electrolyte membrane. On one hand, the membrane should retain high water content to transport protons effectively with low ohmic resistance. Hence, gaseous reactants

(e.g. H_2, O_2) are humidified before being fed into fuel cells. On the other hand, excessive liquid water accumulation within fuel cells would block reactant pathways to reactive sites in catalyst layers, resulting in the so-called flooding situation. Thus, it is evident that there exist two conflicting requirements for liquid water. We need to have a delicate water balance inside fuel cells to ensure that the membrane is fully hydrated for high protonic conductivity, while severe flooding is avoided, especially on the cathode side. To be able to bring about this balance, a profound understanding of water transport inside fuel cells is indispensable [4–7].

It is widely recognized that the flow of two immiscible phases (gas and liquid water) within PEFCs is challenging. While PEFCs are operating under certain conditions (e.g. high current densities, humid environments, and cold start-up), liquid water is simultaneously formed in all components. The mechanisms affecting the liquid water transport are distinct in different layers. A very simple categorization of the two-phase flow in PEFCs can be as follows [8,9]: (1) liquid water accumulation and transport in the CL, (2) two-phase flow in the GDL, along with interfacial coverage at the GC–GDL interface, and (3) water transport in the GC. These three sub-processes negatively impact the performance of PEFCs. For instance, in the CL, excessive liquid water would cover active catalyst sites, acting as an additional barrier to reactants transport. Based on the preceding descriptions of water transport we can see that a proper water management plays a central role in the development and commercialization of PEFCs.

Nomenclature

a	charge transfer coefficient; net water transfer coefficient
A_{gc}	cross-sectional area of gas channel (m^2)
A_m	reactive area (m^2)
C	mass fraction
D	species diffusivity (m^2 s^{-1})
F	Faraday's constant, 96487 (C mol^{-1})
i_0	exchange current density (A m^{-2})
I_{ave}	averaged current density (A m^{-2})
j	volumetric current density (A m^{-3})
k_0	intrinsic permeability (m^2)
k_{rl}	relative permeability for liquid phase
k_{rg}	relative permeability for gas phase
k_{cond}	condensation rate (s^{-1})
k_{evap}	evaporation rate (Pa^{-1} s^{-1})
M	molecular weight (kg mol^{-1})
$\bar{n}$	normal direction vector
n_1	exponent for the effect of liquid water saturation on species diffusivity
n_2	exponent for relative permeabilities
n_3	exponent for the effect of liquid water saturation on current density
p	pressure (Pa)
$p_{H_2O}^{sat}$	water vapor pressure (Pa)
q	switch function for phase change model
R	universal gas constant (8.134 J mol^{-1} K^{-1}); mass source due to phase change (kg m^{-3} s^{-1})
RH	relative humidity
s	liquid water saturation
S	source term
T	temperature (K)
$\bar{V}$	velocity vector (m s^{-1})
$\bar{U}$	intrinsic velocity vector (m s^{-1})
Y	molar concentration (mol m^{-3})

Greek letters

ρ	mass density (kg m^{-3})
ε	porosity
μ	dynamic viscosity (kg m^{-1} s^{-1})
$\bar{\bar{\tau}}$	stress tensor (N m^{-2})
σ	surface tension (N m^{-1})
θ	contact angle (°)
α	cathode catalyst specific area (m^2 m^{-3})
η_c	cathode overpotential (V)
ξ	stoichiometric ratio

Superscripts and subscripts

g	gas phase
l	liquid phase
m	momentum
i	gaseous species index
eff	effective value
c	capillary
ref	reference value
im	immobile
H$_2$O	water vapor
O$_2$	oxygen
sat	saturation
in	inlet

Over the past two decades, the two-phase flow and flooding phenomena in PEFCs have been intensively investigated via both experimental [10–15] and numerical methods [16–25]. To date, several macroscopic computational fluid dynamics (CFD) models for the two-phase flow in PEFCs are available in literature, which are all based on the so-called two-phase Darcy's law [26]. He et al. [27] developed a two-phase flow model for the cathode GDL. They solved a steady-state transport equation of liquid water flow that derived from the two-phase Darcy's law. The equation strongly resembled a general scalar transport equation with convective and diffusive terms. The authors also assumed both capillary diffusivity and convective coefficient to be constants for numerical stability. Following He's method, Ye and Nguyen [29] also derived a similar liquid water transport equation. Single-phase flow methodology was employed to model gas flow, and two phases were coupled by phase change. The effect of the presence of liquid water on gas flow was taken into account only by correcting gaseous species diffusivities. Another popular two-phase model for PEFCs is called multiphase mixture (M^2) model, which has been employed widely by fuel cell researchers [30–34]. Based on the two-phase Darcy's law, the M^2 model for multiphase, multi-component transport in capillary porous media was firstly developed by Wang and coworkers [35,36]. However, several researchers [28,37] used volume-weighted mixture dynamic viscosity and mass-weighted mixture velocity to simplify the M^2 model. So, the applications of this modified M^2 model would be limited. Berning et al. [38] used the so-called multi-fluid model to study liquid water transport in the cathode porous layers. Since this model requires a multiphase solver, and needs to be capable of coupling species transport, phase change, and chemical reactions simultaneously, it entails lots of computational efforts and is prone to being numerically unstable.

In an operating PEFC, liquid water emerges from the GDL into the GC, in the form of small droplets and slugs [6]. These droplets and slugs cover the GDL surface and block the GC, in turn, influence the flooding level inside the diffusion layers. In order to capture this important physical phenomenon, an interactive model of liquid water transport between the GC and GDL should be developed. In most previous studies, a value of interfacial saturation or capillary pressure at the GC–GDL interface was specified. Normally, this value was assigned to zero, corresponding to the mist flow assumption in the GC. However, the mist flow assumption is only valid under high gas flow rates in the GC, which are not encountered in practice. So far, only a few researchers have numerically studied the water coverage effect on cell performance. Song et al. [39] developed a one-dimensional two-phase analytical model to address the effect of liquid water saturation at the GC–GDL interface on the transient behavior of liquid water transport inside the cathode GDL. Results showed that this parameter had a big impact on the calculated water saturation inside the GDL. A more elaborate interfacial coverage model was proposed by Meng and Wang [40]. In their work, the interfacial liquid saturation at the GC–GDL interface was assumed to be a simple function of the GDL surface contact angle, current density, as well as gas inlet velocity. This was not based on a derivation and they also used the mist flow assumption in the GC. The results showed that the interfacial coverage leaded to higher flooding levels inside the GDL and CL. Berning et al. [38] used the Hagen–Poiseuille equation to relate the interfacial water saturation with local pore velocity of liquid water in the GDL. Recently Basu et al. [9] proposed to apply the M^2 model into the GC directly. In this approach, the GC was assumed to be a structured porous medium, and then the two-phase coupling between the GDL and GC became straightforward.

In this work, we develop a two-phase flow model for the cathode side of a PEFC. The GC is assumed to be a structured porous medium with the porosity of 1.0; then, the two-phase Darcy's law is applied to the GC. Based on this model, we study the liquid water flooding
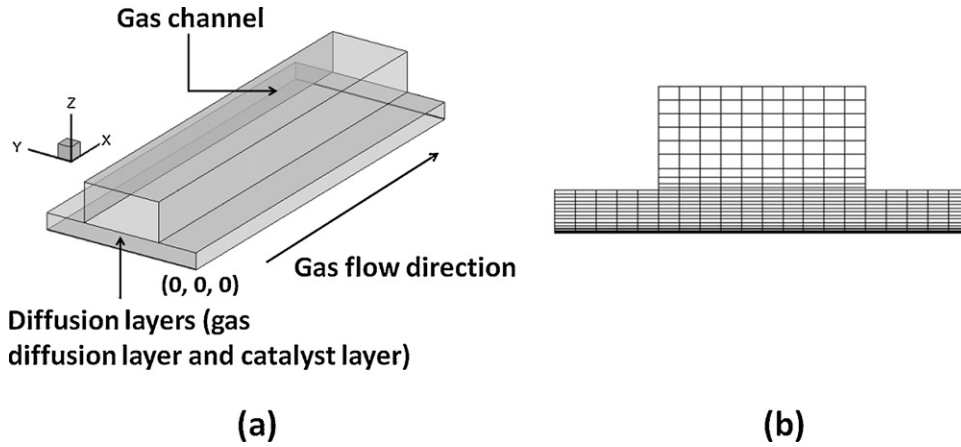
Fig. 1. (a) Computational domain used in this work; (b) and the corresponding mesh in the Y–Z cross-section.

in the GC under different operating conditions, and also its impact on the liquid water distribution in the diffusion layers. Finally, we address the effect of the immobile saturation on the prediction of the liquid water distribution in the diffusion layers.

2. Two-phase flow model

Fig. 1 shows the three-dimensional computational domain and the corresponding mesh in the Y–Z cross-section. In this work, we focus on the liquid water flooding on the cathode side consisting of the CL, GDL and GC. For the sake of simplicity, a micro porous layer is not considered here. The typical cell length of 100 mm is used. In an operating PEFC, humidified air is delivered into the GC and diffuses through the GDL into the CL. There oxygen atoms are formed on the catalyst where they combine with protons from the membrane and electrons from the external circuit to generate liquid water and heat. The following main assumptions are made in our model for numerical simplicity:

(1) Ideal gas mixture
(2) Isotropic and homogeneous diffusion layers
(3) Laminar flow due to small Reynolds numbers and pressure gradients
(4) Isothermal condition.

It is well known and proofed experimentally that the GDL is anisotropic when comparing in-plane and through-plane properties like thermal and electrical conductivities, species diffusivities and permeabilities [41]. Anisotropic thermal and electrical conductivities do not play a role in our model, since heat and electron transport is excluded. According to Tomadakis and Sotirchos [42], the in-plane diffusivity is around 20% larger than the through-plane one. The conclusion indicates that the disregard of the anisotropic diffusivity in this study should not impact the general tendencies of the results. The same argument holds for the permeabilities, since the through-plane permeability of carbon-based GDL is around 50% bigger than the in-plane one [43].

2.1. Governing equations of gas phase

The mass conservation equation of the gas mixture is given as follows:

$$\nabla \cdot (\rho_g \bar{V}_g) = S_g \tag{1}$$

where $\bar{V}_g$ denotes the superficial or Darcy velocity of the gas phase, ρ_g is the density of the gas mixture, and S_g is the mass source term due to the chemical reaction and phase change.

The Darcy velocity is related to the intrinsic or pore-scale velocity by the following definition:

$$\bar{V}_g = (1 - s)\varepsilon \bar{U}_g \tag{2}$$

where $\bar{U}_g$ denotes the intrinsic velocity of the gas phase, ε is the porosity, and s represents the liquid water saturation defined as the volume faction of the pores occupied by the liquid water.

The steady-state momentum equation of the gas phase can be derived based on the two-phase flow methodology [44], which is given as:

$$\frac{1}{\varepsilon^2(1-s)^2} \nabla \cdot (\rho_g \bar{V}_g \bar{V}_g) = -\nabla p_g + \frac{1}{\varepsilon(1-s)} \nabla \cdot (\bar{\bar{\tau}}) + S_m \tag{3}$$

where p_g is the gas phase pressure, $\bar{\bar{\tau}}$ is the stress tensor, and S_m represents the Darcy source term accounting for the viscous resistance imposed by the pore structure of porous media and the presence of liquid water in the pore space.

The above-listed mass and momentum conservation equations of the gas phase are applied to the whole computational domain. Since we regard the GC as a structured porous medium in this work, the porosity of the GC is assumed to be unity. It is worth noting that the two-phase Darcy's law for the gas phase can be obtained by neglecting the inertia and diffusive terms in Eq. (3). However, to keep the same order of the momentum equations used in the GC and diffusion layers, Eq. (3) is adopted in this work.

In automotive applications, we have water vapor, oxygen, and nitrogen species on the cathode side. The species transport equation can be expressed as:

$$\nabla \cdot (\rho_g C_i \bar{V}_g) = \nabla \cdot (\rho_g D_i^{\text{eff}} \nabla C_i) + S_i \tag{4}$$

in which C_i denotes the mass fraction of each component, D_i^{eff} is the effective diffusivity accounting for the presence of liquid water and the pore structure of porous media, and S_i represents the species source term owing to the oxygen reduction reaction (ORR) and phase change. In our calculations, nitrogen is regarded as an inert component.

2.2. Liquid water transport equation

Liquid water is assumed to be a single-component phase, and the gaseous species diffusion in the liquid water is neglected. This is a valid assumption as a first approach since the liquid diffusivities are several orders of magnitudes lower than the gaseous diffusivities. The mass conservation equation of the liquid water is given as:

$$\nabla \cdot (\rho_l \bar{V}_l) = S_l \tag{5}$$

where ρ_l is the liquid water density, S_l is the mass source term, and $\vec{V}_l$ denotes the Darcy velocity of the liquid water, which can be given by the two-phase Darcy's law:

$$\vec{V}_l = -\frac{k_0 k_{rl}}{\mu_l} \nabla p_l \tag{6}$$

Recalling Eq. (3), we can safely drop the inertia and diffusive terms due to their extremely small magnitudes compared to the Darcy term. Then the two-phase Darcy equation for the gas phase is obtained as:

$$\vec{V}_g = -\frac{k_0 k_{rg}}{\mu_g} \nabla p_g \tag{7}$$

In Eqs. (6) and (7), p_l denotes the liquid water pressure, k_0 denotes the intrinsic permeability of porous media, μ_l and μ_g are the dynamic viscosities of the liquid water and gas, respectively, k_{rl} represents the relative permeability for the liquid phase, and k_{rg} represents the relative permeability for the gas phase. The primary difference between these two equations and the single-phase form stems from the presence of the relative permeability, which designates the influence of the reduced void space for each phase due to the existence of the other phase. Finally, the macroscopic capillary pressure is introduced to represent the pressure difference between the gas and liquid phases, given as:

$$p_c(s) = p_g - p_l \tag{8}$$

Eqs. (5)–(8) can be combined, and after a few algebraic manipulations the liquid water transport equation is obtained as:

$$\nabla \cdot \left(\rho_l \frac{k_{rl}}{k_{rg}} \frac{\mu_g}{\mu_l} \vec{V}_g \right) = \nabla \cdot \left(-\rho_l \frac{k_0 k_{rl}}{\mu_l} \nabla p_c \right) + S_l \tag{9}$$

Here, the gas drag effect (the term on the left-hand side) on the liquid water movement and the capillary diffusion (first term on the right-hand side) are both included.

2.3. Constitutive correlations and source terms

To close the governing equations, several constitutive correlations are needed, such as state equation, capillary pressure-saturation and relative permeability-saturation relationships. Ideal gas mixture law is used to calculate the composition-dependent gas phase density as follows:

$$\rho_g = \frac{p_g}{RT \sum_i C_i / M_i} \tag{10}$$

in which, p_g refers to the gas pressure, C_i is the mass fraction of each component, and R is the universal gas constant. Due to the small pressure gradient, the mass density of the liquid water is assumed to be constant.

The multi-component diffusion in the gas phase can be described by Stefan–Maxwell equation. For simplicity, the Fick's law is commonly used [45]. Taking into account the presence of liquid water and the pore structure of porous media, the effective species diffusivity can be given based on Bruggeman correlation:

$$D_i^{eff} = (1-s)^{n_1} \varepsilon^{1.5} D_i \tag{11}$$

where D_i is the molecular diffusivity that depends on the temperature and pressure. For water vapor and oxygen, we have the following empirical expressions [29]:

$$D_{H_2O} = 0.2982 \times 10^{-4} \left(\frac{T}{333} \right)^{1.75} \left(\frac{101,325}{p_g} \right) \tag{12}$$

$$D_{O_2} = 0.2652 \times 10^{-4} \left(\frac{T}{333} \right)^{1.75} \left(\frac{101,325}{p_g} \right) \tag{13}$$

Regarding the capillary pressure, we know that it is dependent on the interface curvature at the micro scale. We traditionally presume that capillary pressure is solely a function of saturation at the macro scale, as expressed in Eq. (8). However, the hysteresis phenomenon of capillary pressure-saturation curves during consecutive drainage and imbibition processes in porous media indicates that other variables may also influence the capillary pressure. Hassanizadeh and Gray [46] claim that, based on a rigorous thermo-dynamical derivation the capillary pressure is not only a function of saturation but also of the specific areas of the three interfaces. However, to date, this model is still hard to be integrated with current CFD codes, since it involves several additional variables. There is also another weakness in the traditional capillary pressure-saturation relationship, which ignores the dynamic effect [47] in the pressure difference between two phases under unsteady state situations. In this work, we still follow the traditional approach, and use the well-known Leverett function, expressed as:

$$p_c = \sigma \, \cos \theta \left(\frac{\varepsilon}{k_0} \right)^{1/2} J(s) \tag{14}$$

$$J(s) = \begin{cases} 1.417(1-s) - 2.120(1-s)^2 + 1.263(1-s)^3 & \text{for } \theta \leq 90° \\ 1.417s - 2.120s^2 + 1.263s^3 & \text{for } \theta > 90° \end{cases} \tag{15}$$

As to the relative permeabilities, power-form correlations are commonly used in the absence of experimental data. They originally come from sand/rock-type porous media with a typical porosity of 0.1–0.4 [29]. Therefore, the relative permeabilities for both gas and liquid phases can be expressed as:

$$k_{rg} = (1-s)^{n_2} \tag{16}$$

$$k_{rl} = \begin{cases} 0 & s < s_{im} \\ s_{eff}^{n_2} & s \geq s_{im} \end{cases} \tag{17}$$

$$s_{eff} = \frac{s - s_{im}}{1 - s_{im}} \tag{18}$$

In these equations, n_2 is the material coefficient, s_{eff} is called the effective saturation, and s_{im} represents the immobile water saturation.

The liquid water flux is assumed to be zero, before it forms conducting pathways in the porous media of interest. As indicated in Eq. (17), when the liquid water saturation is less than the threshold value s_{im}, the relative permeability for the liquid phase is zero; thus, we obtain the zero water flux. Normally, the immobile saturation not only depends on the material properties of porous media, but also can be affected by the flow conditions (such as phase change, boundary condition, and flow history). Only a few researchers [38,48] have investigated the impact of this parameter on the two-phase flow in the diffusion layers of a PEFC using one-dimensional simulations.

The simplified Tafel equation is employed to describe the relatively sluggish ORR in the cathode CL [22]:

$$j_c = (1-s)^{n_3} \alpha i_0^{ref} \frac{C_{O_2}}{Y_{O_2,ref}} \frac{\rho_g}{M_{O_2}} \, \exp \left(\frac{a_c F}{RT} \eta_c \right) \tag{19}$$

Here, the liquid water coverage effect is considered by the exponent n_3, $Y_{O_2,ref}$ denotes the reference molar concentration of oxygen, and η_c is the cathode overpotential.

The phase change between water vapor and liquid water is considered by a nonequilibrium phase change model [49], which is expressed as:

$$R_l = k_{cond} \frac{\varepsilon (1-s) Y_{H_2O} M_{H_2O}}{RT} (Y_{H_2O} p_g - p_{H_2O}^{sat}) q$$
$$+ k_{evap} \varepsilon s \rho_l (Y_{H_2O} p_g - p_{H_2O}^{sat})(1-q) \tag{20}$$

$$q = \frac{1 + \left| Y_{H_2O}p_g - p_{H_2O}^{sat} \right| / (Y_{H_2O}p_g - p_{H_2O}^{sat})}{2} \qquad (21)$$

In Eq. (20), $p_{H_2O}^{sat}$ denotes the water vapor pressure, which can be obtained from the following empirical formula as a function of temperature [44]:

$$\begin{aligned}
\log_{10} \frac{p_{H_2O}^{sat}/101,325}{} = {}&-2.1794 + 0.02953(T - 273.15) \\
&- 9.1837 \times 10^{-5}(T - 273.15)^2 \\
&+ 1.4454 \times 10^{-7}(T - 273.15)^3
\end{aligned} \qquad (22)$$

The source terms of the conservation equations in different regions on the cathode side are listed in Table 1. Since the membrane is not included, the liquid water exchange between the CL and membrane is accounted for by means of the net water transfer coefficient. Note that the generated water in the CL is assumed to be in the liquid form due to the nanostructure of the CL. In this work, we assume the GC to be a structured porous medium associated with a given intrinsic permeability, which can be obtained from numerical experiments or Hagen–Poiseuille law [50].

2.4. Boundary conditions and numerical implementation

The gas inlet velocity on the cathode side can be determined by the specified stoichiometric ratio ξ_c, and the calculated average current density I_{ave}, as follows:

$$I_{ave} = \frac{\int_{CL} j_c dv}{A_m} \qquad (23)$$

$$\bar{V}_{in,g} \cdot \bar{n} = \frac{I_{ave}A_m}{F} \frac{\xi_c}{4Y_{in,O_2}A_{gc}} \qquad (24)$$

where A_m and A_c are the reactive and GC cross-sectional areas, respectively, and Y_{in,O_2} denotes the inlet molar concentration of oxygen, which is determined by the inlet relative humidity RH and local gas pressure, expressed as:

$$Y_{in,O_2} = 0.21 \times \frac{\rho_g}{M_g} \left(1 - \frac{RH \cdot p_{H_2O}^{sat}}{p_g}\right) \qquad (25)$$

The gas pressure at the GC outlet is assumed to be 2 atm. The symmetric boundary conditions are employed at the sidewalls of the GDL and CL due to the repeated structure in a PEFC stack. The slip and impermeable wall conditions are specified at the GC walls, since the GC is assumed to be a structured porous medium. The wall resistance is lumped into the Darcy's source term as shown in Table 1. For the remaining boundaries, the conditions of no-slip and impermeable wall are imposed.

The set of steady-state governing equations and boundary conditions given above are discretized using finite volume method with second-order schemes based on the commercial CFD solver FLUENT. With the aid of user-defined functions, the liquid water transport equation, source terms and constitutive correlations are coupled with the general multi-component gas transport equations. The SIMPLE (semi-implicit method for pressure-linked equations) algorithm is utilized to couple pressure and velocity, and the AMG (algebraic multi-grid) method in conjunction with Gauss-Seidel type smoother is used to solve resultant nonlinear algebraic equations. In all simulations presented in the following section, the scaled values of the equation residuals are smaller than 10^{-6}.

Table 2
Geometrical, physical and operating parameters.

Parameter	Value
GC width/height/length	1.0/0.5/100 mm
Shoulder width	1.0 mm
GDL/CL thickness	0.15/0.015 mm
GC/GDL/CL porosity, ε	1.0/0.6/0.4
GC/GDL/CL intrinsic permeability, k_0	$1.4 \times 10^{-8}/3. \times 10^{-12}/3. \times 10^{-14}$ m²
Cell temperature, T	353.15 K
Operating pressure, p_{ref}	2 atm
n_1/n_3	2.0 /2.0 [9]
GDL /CL /GC n_2	4.0/4.0/5.0 [9]
Liquid water density, ρ_l	972 kg m⁻³
Dynamic viscosity of liquid water/gas mixture, μ	$3.5 \times 10^{-4}/2.03 \times 10^{-5}$ Pa s [29]
Evaporation rate, k_{evap}	5.0×10^{-5} Pa⁻¹ s⁻¹ [29]
Condensation rate, k_{cond}	1.0 s⁻¹ [29]
GC/GDL/CL contact angle, θ	60/120/110°
Surface tension, liquid–water–air, σ	0.0625 N m⁻¹
Charge transfer coefficient, a_c	1.0
Reference current density × ratio of reaction surface to catalyst volume on cathode side, $\alpha i_{0,c}^{ref}$	2.0×10^4 A m⁻³
Reference oxygen molar concentration, $Y_{O_2}^{ref}$	40.88 mol m⁻³
Net water transfer coefficient, a	0.0

3. Results and discussion

Geometrical, physical, and operating parameters are summarized in Table 2. We assume uniform distribution of the cathode overpotential in the CL, and the average current density can be computed from Eq. (23). In what follows, we highlight the importance of modeling GC flooding in the numerical studies of PEFCs. And, its impact on the cell performance and liquid water distribution is explored in detail. At last, we address the effect of immobile saturation on the liquid water distribution in diffusion layers.

3.1. Modeling of GC flooding

In experiments with PEFCs, a large amount of water droplets and slugs forming in the GC are observed, which are finally removed out of the channel mainly due to the gas drag force. In previous numerical studies, two-phase flow in the GC was overwhelmingly simplified by the mist flow assumption. In this work, we apply the two-phase Darcy's law to the GC, and investigate its effect on the cell performance and liquid water distribution. Fig. 2 shows two polarization curves (cathode potential vs. current density) under
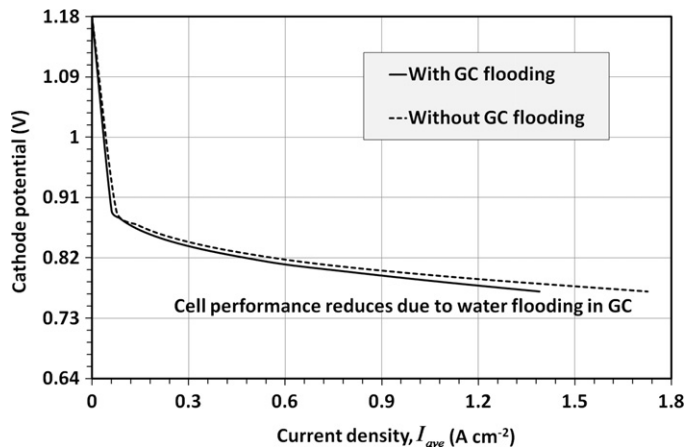
Fig. 2. Polarization curves (cathode potential vs. current density) taking into account GC flooding, and neglecting GC flooding. It is clearly seen that the cell performance reduces due to the liquid water flooding in the GC.

Table 1
Source terms of the conservation equations in different regions on the cathode side.

Computational domain	S_g	S_m	S_{O_2}	S_{H_2O}	S_l
GC	$-R_l$	$-\frac{\mu_g}{k_{GC}k_{rg}}\vec{V}_g$	0	$-R_l$	R_l
GDL	$-R_l$	$-\frac{\mu_g}{k_{GDL}k_{rg}}\vec{V}_g$	0	$-R_l$	R_l
CL	$-R_l - \frac{j_c}{4F}M_{O_2}$	$-\frac{\mu_g}{k_{CL}k_{rg}}\vec{V}_g$	$-\frac{j_c}{4F}M_{O_2}$	$-R_l$	$R_l + \frac{j_c(1+2a)}{2F}M_{H_2O}$

the situations of considering the GC flooding, and neglecting the GC flooding, separately. It can be seen that neglecting the GC flooding would overestimate the cell performance. We also validate our model against experimental data in terms of gas pressure drop in the GC [6,9]. Based on an operating PEFC, Hussaini et al. [6] measured the gas pressure drops under different flooding situations in the GC. In our simulations, the same GC dimensions (see Table 2) and operating conditions (RH = 66%) as in Ref. [6] are used. Comparisons of numerical and experimental results are shown in Fig. 3. The excellent match is obtained at the current density of 0.5 A cm^{-2}. Increasing the stoichiometric ratio does not invoke obvious increase of the gas pressure drop, since more liquid water can be swept out of the channel under the higher gas flow rate. However, our model overpredicts the gas pressure drops at the current density of 0.8 A cm^{-2}, and underestimates the gas pressure drops at the low current density of 0.2 A cm^{-2}, respectively. This may be partly due to the unresolved water exchange between the cathode and anode sides in our half cell model. It also needs to point out that our channel flooding model is capable of predicting the tendency of gas pressure drop as increasing the stoichiometric ratio, as shown in Fig. 3.

Fig. 4 shows the comparison of the liquid water distributions at the middle cross-section ($Y = 1 \times 10^{-3}$ m) of the cathode side under two situations: considering the GC flooding (Fig. 4a), and neglecting the GC flooding (Fig. 4b). The corresponding operating conditions are as follows: RH = 66%, $\xi_c = 2.0$, $s_{im} = 0$, and $I_{ave} = 0.2$ A cm^{-2}. Much more liquid water is found in the diffusion layers due to the water coverage effect at the GC–GDL interface. The cathode overpotential increases to 0.392 V when taking into account the GC flooding. This indicates the decreased cell performance.

At the same operating conditions, the liquid water distributions at the middle cross-section ($Z = 9.0 \times 10^{-4}$ m) of the GDL are plotted in Fig. 5. The liquid water saturation at the inlet portions is zero due to the partially humidified air feeding. When neglecting the GC flooding (Fig. 5b) more liquid water is found under the land, this is because the liquid water under the land has to travel a somewhat
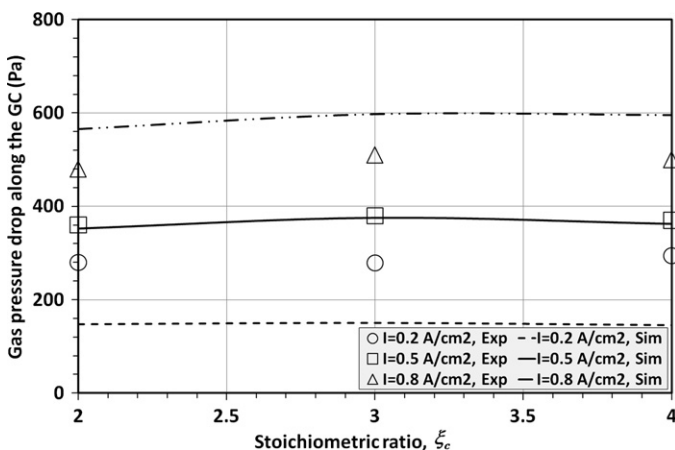

Fig. 4. Distributions of the liquid water saturation at the middle cross-section ($Y = 1.0 \times 10^{-3}$ m) of the cathode side (operating conditions: RH = 66%, $\xi_c = 2.0$, $s_{im} = 0$, and $I_{ave} = 0.2$ A cm^{-2}).

longer path to reach the GC. The liquid water saturation reduces slightly along the flow direction owing to the decreased current density. When the GC flooding model is included, the liquid water saturation increases along the flow direction (Fig. 5a). This opposite water distribution indicates that the GC flooding impacts the liquid water distribution in the diffusion layers considerably. Neglecting the GC flooding would lead to the incorrect prediction of liquid water distribution in the diffusion layers. In addition, the liquid water distribution in the transverse direction of the GC is more uniform, which is also caused by the presence of liquid water in the GC.

Fig. 6a shows the liquid water distributions at the middle cross-section ($X = 0.05$ m) of the cathode side. Liquid water flooding in the GC results in almost even distribution of the liquid water at the cross-section (left). However, a distinct gradient of the liquid water saturation is found when we neglect the liquid water flooding in the GC (right). Fig. 6b displays the distributions of the mole fraction of oxygen at the same cross-section. Lower oxygen concentrations are found under the land due to the transport limitation. When considering the GC flooding, much more liquid water is present in

Fig. 3. Gas pressure drop validation at different current densities and stoichiometric ratios (experimental data are extracted from Ref. [9]).
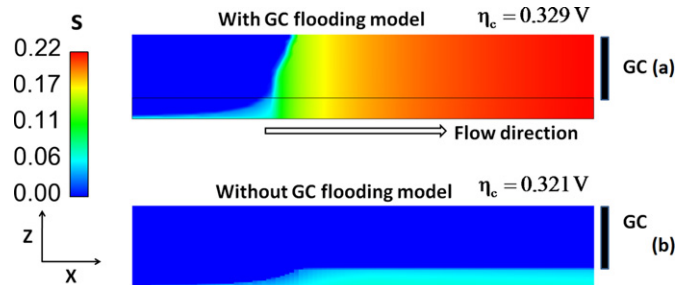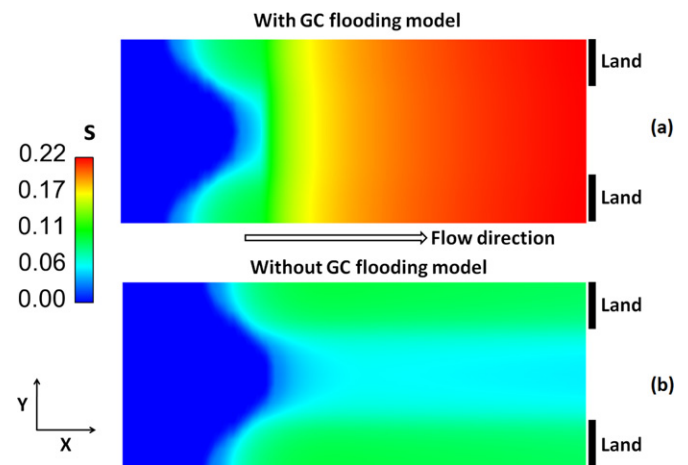

Fig. 5. Distributions of the liquid water saturation at the middle cross-section ($Z = 9.0 \times 10^{-5}$ m) of the GDL (operating conditions: RH = 66%, $\xi_c = 2.0$, $s_{im} = 0$, and $I_{ave} = 0.2$ A cm^{-2}).
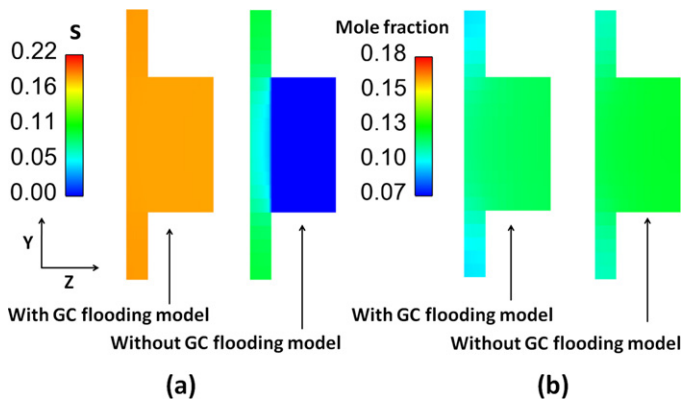
Fig. 6. Distributions of (a) the liquid water saturation, (b) the mole fraction of oxygen at the middle cross-section ($X = 0.05$ m) of the cathode side (operating conditions: RH = 66%, $\xi_c = 2.0$, $s_{im} = 0$, and $I_{ave} = 0.2$ A cm^{-2}).

the diffusion layers (Fig. 6a). This gives rise to the higher oxygen diffusion resistance. Therefore, even lower oxygen concentration is observed (Fig. 6b, left one).

Fig. 7 illustrates the influence of the stoichiometric ratio on the liquid water distribution at the middle cross-section ($Z = 4.15 \times 10^{-4}$ m) of the GC. The operating conditions are: RH = 66%, $s_{im} = 0$, and $I_{ave} = 0.5$ A cm^{-2}. When the applied stoichiometric ratio equals to 2.0, the highest liquid water saturation is predicted to be 0.23 at the end of the GC (Fig. 7a). We also can observe the water vapor front at which the water vapor reaches its saturated value. With the increase of the stoichiometric ratio, the liquid water flooding is mitigated in the GC. This can be explained by the fact that more liquid water is removed out of the GC with the increase of the gas flow rate. Meanwhile, the water vapor front moves fast towards the end of the GC, which indicates that more water is transported out of the GC in the water vapor form. When the applied stoichiometric ratio equals to 4.0, only a little liquid water is left at the end of the GC. And, the cathode overpotential decreases to 0.348 V, indicative of the increased cell performance.

Fig. 8 illustrates the influence of the inlet air relative humidity on the liquid water distribution at the middle cross-section ($Z = 4.15 \times 10^{-4}$ m) of the GC. Three different values of relative
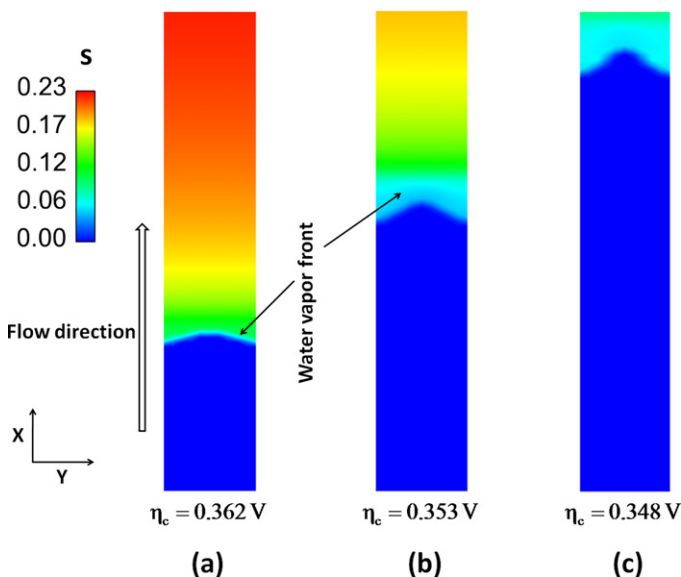

Fig. 7. Distributions of the liquid water saturation at the middle cross-section ($Z = 4.15 \times 10^{-4}$) of the GC at different stoichiometric ratios: (a) $\xi_c = 2.0$, (b) $\xi_c = 3.0$, (c) and $\xi_c = 4.0$ (operating conditions: RH = 66%, $s_{im} = 0$, and $I_{ave} = 0.5$ A cm^{-2}).
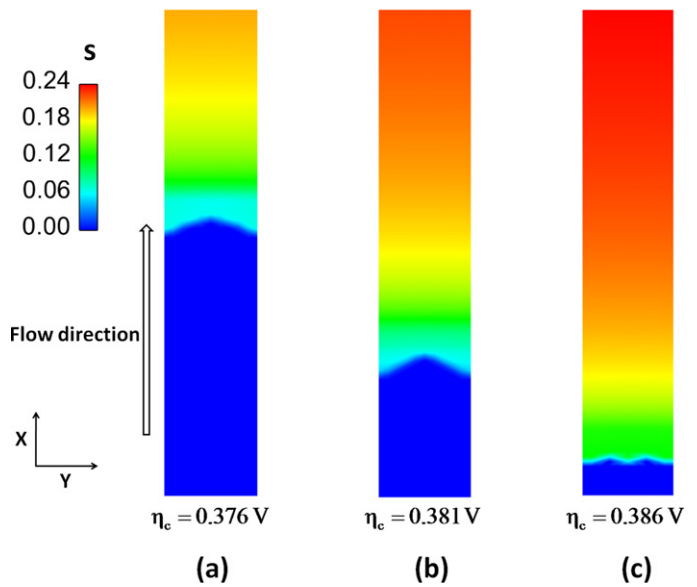

Fig. 8. Distributions of the liquid water saturation at the middle cross-section ($Z = 4.15 \times 10^{-4}$) of the GC at different inlet relative humidity: (a) RH = 46%, (b) RH = 66%, (c) and RH = 86% (operating conditions: $\xi_c = 2.0$, $s_{im} = 0$, and $I_{ave} = 0.8$ A cm^{-2}).

humidity are assigned, namely, 46%, 66%, and 86%. The operating conditions are: $\xi_c = 2.0$, $s_{im} = 0$, and $I_{ave} = 0.8$ A cm^{-2}. At the low relative humidity of 46% (Fig. 8a), only less than half GC is flooded by the liquid water, and most generated water is removed out of the GC in the water vapor form as mentioned above. As a consequence, we get the minimum cathode overpotential of 0.376 V in all three cases. However, it is worth noting that low relative humidity would result in the membrane dehydration mainly at the inlet portion, which decreases the cell performance. From Fig. 8, we also can see that more and more liquid water accumulates in the GC with the increase of the inlet relative humidity. Although increasing the inlet relative humidity can slightly increase the gas flow rate at the same current density and stoichiometric ratio, the phase change dominates the liquid water flooding in the GC. Therefore, we obtain the maximum water saturation up to 0.24, when the inlet relative humidity equals to 86% (Fig. 8c). And, almost all the GC is flooded by the liquid water. Comparison between Fig. 8b and Fig. 7a shows that increasing the current density from 0.5 to 0.8 A cm^{-2} gives the indiscernible change of the GC flooding. This is attributed to the fact that the high current density corresponds to the high gas flow rate, which can drag more liquid water out of the channel.

In this work, we apply Eq. (9) to track the liquid water flooding in the GC as a first attempt. By examining Eq. (9), we can see that two mechanisms determine the liquid water transport in the GC, namely, gas drag force and capillary action. However, their magnitudes strongly depend on the assumed material properties, such as GC contact angle and relative permeability for each phase. In what follows, we evaluate the sensitivity of the simulated GC flooding to these assumed material properties. Fig. 9 shows the contact angle effect on the liquid water distribution at the middle cross-section ($Z = 4.15 \times 10^{-4}$ m) of the GC. It needs to note that the real GC normally comprises of the hydrophilic sidewalls and is enclosed by the hydrophobic GDL surface. However, in this work, we lump all the wettability features to a GC contact angle. From Fig. 9 it can be seen that the liquid water flooding in the GC is insensitive to the contact angle at the fixed cathode overpotential of 0.38 V. This indicates that the capillary action is not the dominant mechanism of the liquid water transport in the GC.

Fig. 10 demonstrates the sensitivity of the liquid water flooding to the gas drag coefficient in the GC. According to Eq. (9), we can
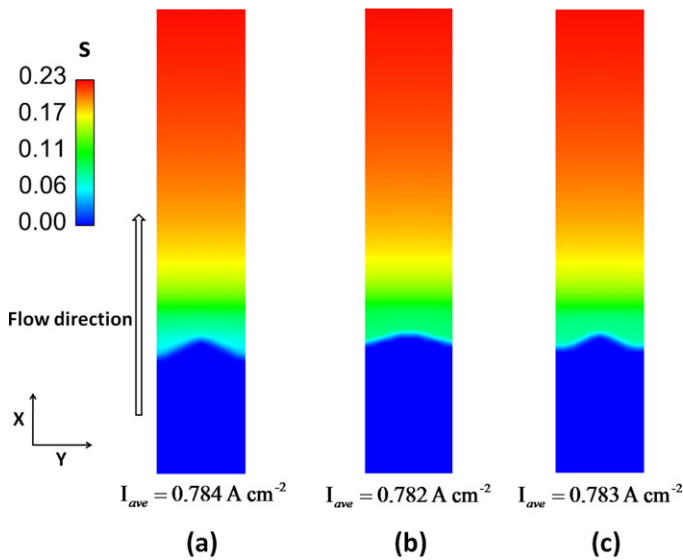
Fig. 9. Distributions of the liquid water saturation at the middle cross-section ($Z = 4.15 \times 10^{-4}$) of the GC at different GC contact angles: (a) $\theta = 60°$, (b) $\theta = 80°$, and (c) $\theta = 110°$ (operating conditions: RH = 66%, $\xi_c = 2.0$, $s_{im} = 0$, and $\eta_c = 0.38$ V).

see that the gas drag effect is directly determined by the relative permeabilities for both phases in the GC. By adjusting the exponent n_2 in the definition of the relative permeability, we can evaluate the gas drag effect on the liquid water flooding in the GC. Fig. 10 shows that the GC flooding is very sensitive to the applied material property n_2. With the decrease of n_2, more and more liquid water is swept out of the channel by the gas flow. This indicates that proper estimation of the gas drag force is crucial to the GC flooding model used in this work. When the GC is assumed to be a structured porous media, the nominal relative permeability for each phase cannot be only a function of water saturation, but also of other variables (e. g. gas flow rate and current density). Maybe experimental data can help fit an empirical formulation.

3.2. Immobile saturation effect

The immobile saturation could be an important parameter in the modeling of liquid water transport in the diffusion layers. Before the liquid water forms conducting pathways (i.e. the water saturation is less than s_{im}), its relative permeability equals to zero; otherwise,
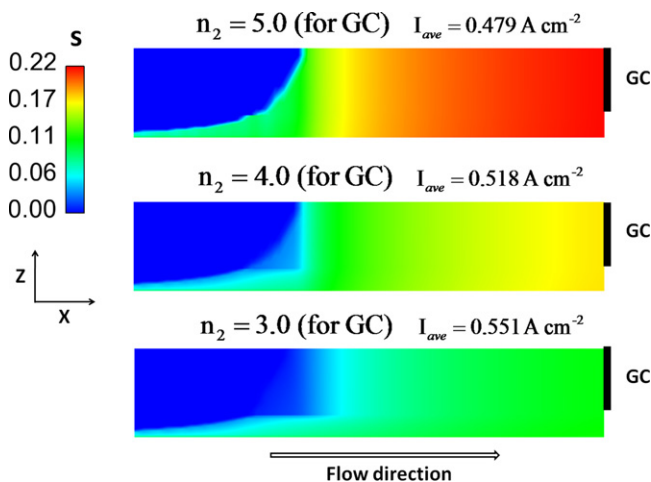

Fig. 10. Impact of the gas drag coefficient on the water saturation distributions at the middle cross-section ($Y = 1.0 \times 10^{-3}$ m) of the cathode side (operating conditions: RH = 66%, $\xi_c = 2.0$, $s_{im} = 0$, and $\eta_c = 0.36$ V).
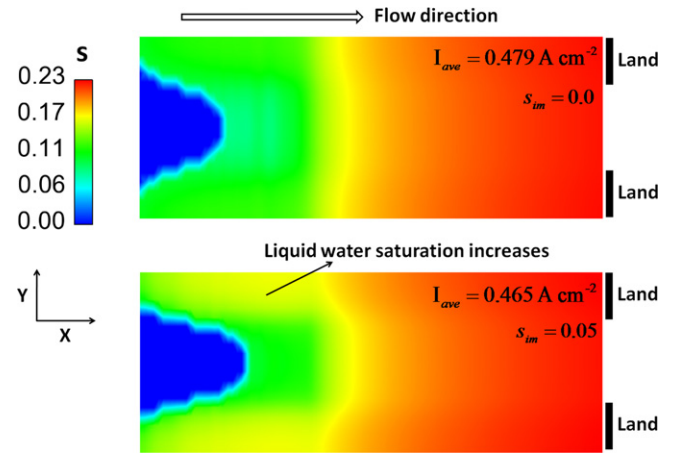

Fig. 11. Effect of the immobile saturation on the liquid water distribution at the middle cross-section ($Z = 9.0 \times 10^{-5}$ m) of the GDL (operating conditions: RH = 66%, $\xi_c = 2.0$, and $\eta_c = 0.36$ V).

the effective saturation is employed in the relative permeability-saturation correlation. Since the gas phase is always continuous throughout the whole domain, its relative permeability is given by Eq. (16). Ju [48] used the effective saturation in the capillary pressure–saturation correlation. However, it is better to work with the actual water saturation s as shown in Eq. (15).

As stated earlier, the immobile saturation depends on the flow conditions and microstructure of porous media, normally an approximate value is assigned to it. In this work, we assign a constant value of 0.05 to the immobile saturation, and investigate its effect on the liquid water distribution in the diffusion layers. It needs to point out that when the immobile saturation is taken into account, the exponent n_2 should be corrected to fit experimental data. However, due to the absence of experimental data, we keep it unchanged as a first attempt.

Fig. 11 shows the effect of the immobile saturation on the liquid water distribution at the middle cross-section ($Z = 9.0 \times 10^{-5}$) of the GDL. The operating conditions are: RH = 66%, $\xi_c = 2.0$, and $\eta_c = 0.36$ V. When considering the immobile saturation (lower one), more liquid water resides in the diffusion layers. As a result, the current density decreases slightly. Unlike the GC flooding, the immobile saturation does not change the tendency of the liquid water distribution along the flow direction. It only increases the flooding level in the diffusion layers.

4. Conclusions

A two-phase flow model for the cathode side of a PEFC has been developed in this work. The salient feature is that we assume the GC to be a structured porous medium; then, the liquid water flooding in the GC can be modeled by the two-phase Darcy's law as a first attempt. We investigate the GC flooding under different operating conditions, and its impact on the liquid water distribution in the diffusion layers. We also study the effect of the immobile saturation on the predicted liquid water distribution in the diffusion layers. The main findings and conclusions are summarized in the following:

(1) Neglecting the GC flooding leads to the incorrect prediction of the liquid water distribution in the diffusion layers, and also overestimates the cell performance.
(2) Increasing the stoichiometric ratio does not invoke obvious increase of the gas pressure drop in the GC, since more liquid water can be removed out of the channel under the higher gas

flow rate. This indicates that practically we can optimize the gas flow rate to achieve the best cell performance.

(3) Decreasing the relative humidity of the inlet gas can mitigate the GC flooding, since more liquid is transported out of the channel in the water vapor form. However, a proper selection of relative humidity is needed to balance two requirements: preventing the membrane dehydration, and mitigating the GC flooding.

(4) The gas flow is the main driving force for the liquid water transport in the GC. The liquid water flooding in the GC is insensitive to the capillary action.

(5) When considering the immobile saturation in the model, more liquid water is predicted to be in the diffusion layers, and the cell performance decreases slightly.

References

[1] M.M. Mench, Fuel Cell Engines, John Wiley & Sons, 2008.
[2] G. Hoogers, Fuel Cell Technology Handbook, CRC Press, 2003.
[3] C.Y. Wang, Chem. Rev. 104 (2004) 4727–4765.
[4] H. Li, Y. Tang, Z. Wang, J. Power Sources 178 (2008) 103–117.
[5] A.Z. Weber, J. Newman, Chem. Rev. 104 (2004) 4679–4726.
[6] I.S. Hussaini, C.Y. Wang, J. Power Sources 187 (2009) 444–451.
[7] I. Manke, C. Hartnig, M. Grünerbel, et al., Appl. Phys. Lett. 90 (2007) 174105.
[8] Y. Wang, S. Basu, C.Y. Wang, J. Power Sources 179 (2008) 603–617.
[9] S. Basu, J. Li, C.Y. Wang, J. Power Sources 187 (2009) 431–443.
[10] I. Manke, C. Hartnig, N. Kardjilov, et al., Appl. Phys. Lett. 92 (2008) 244101.
[11] R. Satija, D.L. Jacobson, M. Arif, S.A. Werner, J. Power Sources 129 (2004) 238–245.
[12] T. Ous, C. Arcoumanis, J. Power Sources 187 (2009) 182–189.
[13] F.Y. Zhang, X.G. Yang, C.Y. Wang, J. Electrochem. Soc. 153 (2006) A225–A232.
[14] B. Gao, T.S. Steenhuis, Y. Zevi, et al., J. Power Sources 190 (2009) 493–498.
[15] I.S. Hussaini, C.Y. Wang, J. Power Sources 195 (2010) 3830–3840.
[16] B.R. Sivertsen, N. Djilali, J. Power Sources 141 (2005) 65–78.
[17] N. Djilali, Energy 32 (2007) 269–280.
[18] K.J. Lee, J.H. Nam, C.J. Kim, Electrochim. Acta 54 (2009) 1166–1176.
[19] L. Mao, C.Y. Wang, Y. Tabuchi, J. Electrochem. Soc. 154 (2007) B341–B351.
[20] P. Zhou, C.W. Wu, J. Power Sources 195 (2010) 1408–1415.
[21] P.K. Sinha, P.P. Mukherjee, C.Y. Wang, J. Mater. Chem. 17 (2007) 3089–3103.
[22] T. Berning, N. Djilali, J. Electrochem. Soc. 150 (12) (2003) A1589–A1598.
[23] X.D. Niu, T. Munekata, S.A. Hyodo, K. Suga, J. Power Sources 172 (2007) 542–552.
[24] X. Liu, W. Tao, Z. Li, Y. He, J. Power Sources 158 (2006) 25–35.
[25] Z. Shi, X. Wang, J. Power Sources 185 (2008) 985–992.
[26] G.F. Pinder, W.G. Gray, Essentials of Multiphase Flow and Transport in Porous Media, John Wiley & Sons, 2008.
[27] W. He, J.S. Yi, T.V. Nguyen, AIChE J. 46 (2000) 2053–2064.
[28] W. Yuan, Y. Tang, M. Pan, Z. Li, B. Tang, Renew. Energy 35 (2010) 656–666.
[29] Q. Ye, T.V. Nguyen, J. Electrochem. Soc. 154 (2007) B1242–B1251.
[30] V. Guran, R.V. Edwards, J.A. Mann, et al., Electrochem. Solid-State Lett. 11 (2008) B132–B135.
[31] C.Y. Wang, Electrochem. Solid-State Lett. 12 (2009) S2–S3.
[32] Y. Wang, J. Power Sources 185 (2008) 261–271.
[33] H. Meng, J. Power Sources 164 (2007) 688–696.
[34] Y. Wang, C.Y. Wang, K.S. Chen, Electrochim. Acta 52 (2007) 3965–3975.
[35] C.Y. Wang, P. Cheng, Int. J. Heat Mass Transfer 39 (1996) 3607–3618.
[36] C.Y. Wang, C. Bechermann, Int. J. Heat Mass Transfer 36 (1993) 2747–2758.
[37] N. Khajen-Hosseini-Dalasm, K. Fushinobu, K. Okazaki, J. Power Sources 195 (2010) 7003–7010.
[38] T. Berning, M. Odgaard, S.K. Kær, J. Eletrochem. Soc. 156 (2009) B1301–B1311.
[39] D. Song, Q. Wang, Z.S. Liu, C. Huang, J. Power Sources 159 (2006) 928–942.
[40] H. Meng, C.Y. Wang, J. Electrochem. Soc. 152 (2005) A1733–A1741.
[41] H. Ju, J. Power Sources 191 (2009) 259–268.
[42] M.M. Tomadakis, S.V. Sotirchos, AIChE J. 39 (1993) 397–412.
[43] U. Pasaogullari, P.P. Mukherjee, C.Y. Wang, K.S. Chen, J. Eletrochem. Soc. 154 (2007) B823–B834.
[44] X. Liu, G. Lou, Z. Wen, J. Power Sources 195 (2010) 2764–2773.
[45] J.E. Dawes, N.S. Hanspal, O.A. Family, A. Turan, Chem. Eng. Sci. 64 (2009) 2781–2794.
[46] S.M. Hassanizadeh, W.G. Gray, Adv. Water Res. 13 (1990) 169–186.
[47] S.M. Hassanizadeh, M.A. Celia, H.K. Dahle, Vadose Zone J. 1 (2002) 38–57.
[48] H. Ju, J. Power Sources 185 (2008) 55–62.
[49] G. Lin, W. He, T.V. Nguyen, J. Electrochem. Soc. 151 (2004) A1999–A2006.
[50] N.A. Mortensen, F. Okkels, H. Bruus, Phys. Rev. E 71 (2005) 057301.